Co-simulation coupling spectral/finite elements for 3D soil/structure interaction problems

Loïc Zuchowski [a], Michael Brun [a,*], Florent De Martin [b]

[a] *Université de Lyon, INSA-Lyon, SMS, 34, rue des Arts, 69621 Villeurbanne, France*
[b] *BRGM (French Geological Survey), 3 avenue Claude-Guillemin, 45060 Orléans, France*

A B S T R A C T

The coupling between an implicit finite elements (FE) code and an explicit spectral elements (SE) code has been explored for solving the elastic wave propagation in the case of soil/structure interaction problem. The coupling approach is based on domain decomposition methods in transient dynamics. The spatial coupling at the interface is managed by a standard coupling mortar approach, whereas the time integration is dealt with an hybrid asynchronous time integrator. An external coupling software, handling the interface problem, has been set up in order to couple the FE software Code_Aster with the SE software EFISPEC3D.

© 2018 Académie des sciences. Published by Elsevier Masson SAS. This is an open access article under the CC BY-NC-ND license (http://creativecommons.org/licenses/by-nc-nd/4.0/).

1. Introduction

Among the different numerical approaches for solving the wave propagation problem, the spectral element method (SEM) with explicit time integration offers the flexibility of the classical finite element method (FEM) for dealing with quite complex geometries, anisotropy and free-surface condition, while minimizing the computational cost thanks to its efficient quadrature formulation and its high-order polynomial accuracy to approximate smooth solutions. The SEM was first developed in computational fluid dynamics [1] and applied in the late nineties for wave propagation in 3D earth media by Komatitsch and co-authors [2,3]. The application of a SEM on soil/structure interaction problems has not been investigated yet because the zone of interest of the soil/structure interaction is geometrically complex and may experience non-linear soil/structure behaviors that are hardly handled by the explicit integration scheme of a SEM. Indeed, the SEM is desirable for modeling the wave propagation at large scale, while the FEM deals with the soil/structure interaction problem at smaller scale. Thus, the SEM and FEM approaches have their own advantages for simulating a soil/structure interaction problem, advocating for an hybrid approach enabling to use both methods in the same simulation. More precisely, the goal of this work is to propose a co-simulation strategy, in which SEM and FEM numerical codes are coupled.

The coupling is based on domain decomposition method with non-overlapping subdomains, using a dual approach with the introduction of Lagrange multipliers in order to connect the different meshes. Multi-time step explicit/implicit co-simulations have been proposed by the authors in previous papers in the case of structure/structure coupling in non-linear dynamics (earthquake and blast loading, [4–6]), fluid structure interaction problem [7], and contact mechanics [8]. Coupling methods have been developed in [9] and [10] based on energy considerations, ensuring the stability and accuracy of the cou-

---

* Corresponding author.
E-mail addresses: loic-l.zuchowski@edf.fr (L. Zuchowski), michael.brun@insa-lyon.fr (M. Brun), F.DeMartin@brgm.fr (F. De Martin).
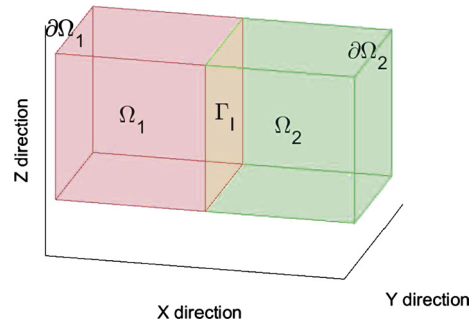
Fig. 1. Ω_1 and Ω_2 3D subdomains with a flat interface Γ_I.

pling scheme. In the case of non-matching interface and different spatial discretizations in subdomains, the mortar coupling approach was proposed by Bernardi et al. [11] for connecting finite element meshes to spectral element meshes in solid mechanics. Casadei et al. [12] proposed an hybrid approach using the mortar coupling method to deal with soil/structure interaction problem, demonstrating the accuracy, robustness and flexibility of the SEM/FEM coupling approach. However, the coupling approach is not a co-simulation, because it is implemented in only one explicit FEM code, Europlexus, with a unique time step. The aim of this paper is to set up a coupling strategy enabling to use an explicit SEM code, EFISPEC3D [13], with an implicit FEM code, Code_Aster [14], while considering different time scales for the time integration. The paper is organized as follows: Section 2 presents the general statement of the soil/structure interaction problem of interest as well as the weak form of the domain decomposition problem that contains the common formalism of the following spatial discretizations; Section 3 provides a brief review of the spatial FEM and SEM discretizations and gives the mortar coupling terms in the weak form of the global problem, related to the interface between the subdomains; Section 4 is devoted to the hybrid (explicit/implicit) asynchronous (different time steps) time integration adopted for the EFISPEC3D/Code_Aster co-simulation; finally, in Section 5, 3D numerical tests employing hexahedral elements in both SEM and FEM partitions are presented in order to demonstrate the accuracy and flexibility of the proposed approach.

2. Problem statement

2.1. Domain decomposition for SEM/FEM coupling

The purpose of this work is to set up a FEM/SEM coupling approach in order to deal efficiently with soil/structure interaction problems. Let Ω a bounded domain belonging to $\mathbb{R}^d$ with a regular boundary, d being the number of space dimensions assumed to be equal to 3 in the following. $J = [0, T]$ is the time interval of interest. As illustrated in Fig. 1, we assume that the domain Ω is divided into two parts Ω_1 and Ω_2 such as: $\Omega_1 \cap \Omega_2 = \emptyset$ and $\partial\Omega_1 \cap \partial\Omega_2 = \Gamma_I$. Γ_I represents the interface between the two subdomains. For both subdomains, we assume the classical partition of the boundary $\partial\Omega_i$ between the Dirichlet boundary, the Neumann boundary and the interface boundary, denoted by Γ_i^D, Γ_i^N and Γ_I, respectively: $\partial\Omega_i = \Gamma_i^D \cup \Gamma_i^N \cup \Gamma_I$.

It is assumed that both subdomains Ω_1 and Ω_2 are characterized by the density ρ_1, ρ_2 and the Lamé coefficients λ_{L_1}, μ_{L_1} and λ_{L_2}, μ_{L_2}. E_1, ν_1 and E_2, ν_2 are Young's modulus and Poisson's ratio. The purpose of this section is to set up the formulation of the coupling between the two subdomains related to different numerical approaches:

- Ω_1 solved by the Finite Element Method (FEM) dealing with the structure and its surrounding soil, corresponding to the zone of interest,
- Ω_2 solved by the Spectral Element Method (SEM) dealing with the soil regions sufficiently far away from the zone of interest.

The SEM partition is assumed to remain linear elastic (small-displacement behavior and elastic linear materials) because the SEM takes full profit of the linear assumption, enabling to drastically reduce the computation time. The FEM partition is also assumed to be linear elastic in the following presentation. However, in practical soil/structure interaction, both structure and surrounding soil are prone to exhibit strong site effects, characterized by material non linearities such as damage and plasticity, large displacements, large strains or contact/friction phenomena. As a result, it is suitable to include such non-linearities in the FEM subdomain, whereas the SEM regions should remain linear elastic or viscoelastic. The extension of the proposed FEM/SEM co-simulation strategy to non-linear behavior in the FEM partition is planned in future works.

2.2. Strong form for the coupling problem

The wave motion in both subdomains Ω_i, $i = 1, 2$, is governed by the following system of equations:

$$
\begin{cases}
\operatorname{div}(\underline{\underline{\sigma}}_i) + \underline{b}_i = \rho_1 \underline{\ddot{u}}_i & \text{in } \Omega_i \times J \\
\underline{\underline{\sigma}}_i = \underline{\underline{\underline{C}}}_i : \underline{\underline{\varepsilon}}_i & \text{in } \Omega_i \times J \\
\underline{\underline{\varepsilon}}_i = \frac{1}{2} \left[\operatorname{grad}(\underline{u}_i) + \operatorname{grad}(\underline{u}_i)^{\mathsf{T}} \right] & \text{in } \Omega_i \times J
\end{cases}
\tag{1}
$$

with the boundary conditions:

$$
\begin{cases}
\underline{u}_i = \underline{u}_i^{\mathrm{D}} & \text{on } \Gamma_i^{\mathrm{D}} \times J \\
\underline{\underline{\sigma}}_i \cdot \underline{n}_i = \underline{g}_i^{\mathrm{N}} & \text{on } \Gamma_i^{\mathrm{N}} \times J
\end{cases}
\tag{2}
$$

where $\underline{b}_i$ is the body force per unit volume, $\underline{\underline{\sigma}}_i$ and $\underline{\underline{\varepsilon}}_i$ are the second-order stress and strain tensors, $\underline{\underline{\underline{C}}}_i$ is the fourth-order elastic constitutive tensor, $\underline{u}_i^{\mathrm{D}}$ is the Dirichlet prescribed displacement, $\underline{n}_i$ is the unit outer normal vector to the boundary and $\underline{g}_i^{\mathrm{N}}$ the traction force.

The initial conditions are given as:

$$
\left\{ \underline{u}_i(t = 0) = \underline{u}_{i,0} \quad \text{in } \Omega_i \right.
\tag{3}
$$

On the interface Γ_I between the two subdomains, the coupling condition can be expressed in its strong form:

$$
\begin{cases}
\underline{v}_1 = \underline{v}_2 & \text{on } \Gamma_I \times J \\
\underline{\underline{\sigma}}_1 \cdot \underline{n}_1 + \underline{\underline{\sigma}}_2 \cdot \underline{n}_2 = 0 & \text{on } \Gamma_I \times J
\end{cases}
\tag{4}
$$

The above equation states the continuity of velocities and the equilibrium of traction forces at the interface. It is important to note that kinematic continuity is prescribed here in terms of velocities rather than in terms of displacements as usual. At this point, there is no difference in the continuous setting in prescribing the continuity of displacements, velocities or accelerations, but it is not true in the discrete setting. It will be underlined in the following that adopted hybrid multi time step integration should be based on the velocity continuity at the interface in order to ensure the stability of the coupling scheme.

3. Spatial discretization of the coupling problem

3.1. Weak form for the coupling problem

The weak form for the whole domain Ω requires the introduction of the test functions in the partitions Ω_1 and Ω_2, belonging to the appropriate spaces. Classically, in the weak form of the wave propagation problem, we define the solution spaces and the test function spaces. The solutions $\underline{u}_1(t)$ and $\underline{u}_2(t)$ in subdomains Ω_1 and Ω_2 are sought in the appropriate spaces $V_1 = \left\{ \underline{u}_1 \in [H^1(\Omega_1)]^d : \underline{u}_1 = \underline{u}_1^{\mathrm{D}} \text{ on } \Gamma_1^{\mathrm{D}} \right\}$ and $V_2 = \left\{ \underline{u}_2 \in [H^1(\Omega_2)]^d : \underline{u}_2 = \underline{u}_2^{\mathrm{D}} \text{ on } \Gamma_2^{\mathrm{D}} \right\}$, respectively, whereas the test space functions $\underline{v}_1$ and $\underline{v}_2$ belong to the spaces V_1^0 and V_2^0, satisfying the zero value at the Dirichlet conditions.

The gluing between the subdomains Ω_1 and Ω_2 is ensured via Lagrange multipliers defined on the interface according to a dual Schur approach. So we introduce the Lagrange multiplier field $\underline{\lambda}$ defined on the interface Γ_I. The coupling between the partitions is realized in a weak way, by following a standard mortar approach [11]. For this purpose, we consider the Lagrange multipliers $\underline{\lambda}$ as well as its related test functions $\underline{\mu}$, belonging to the appropriate spaces, corresponding to the adapted dual trace space denoted by M.

Now, we can express the principle of virtual power for transient structural dynamics problems coupling two subdomains with a dual Schur approach: $\forall t \in J$, find the solution $\underline{u}_1(t) \in V_1$, $\underline{u}_2(t) \in V_2$ and $\underline{\lambda}(t) \in M$, for which the following weak form is satisfied $\forall \underline{v}_1 \in V_1^0$, $\forall \underline{v}_2 \in V_2^0$ and $\forall \underline{\mu} \in M$:

$$
\int_{\Omega_1} \rho_1 \underline{v}_1 \cdot \underline{\ddot{u}}_1 \mathrm{d}\Omega + \int_{\Omega_1} \underline{\underline{\varepsilon}}(\underline{v}_1) : \underline{\underline{\sigma}}_1 \mathrm{d}\Omega + \int_{\Omega_2} \rho_2 \underline{v}_2 \cdot \underline{\ddot{u}}_2 \mathrm{d}\Omega + \int_{\Omega_2} \underline{\underline{\varepsilon}}(\underline{v}_2) : \underline{\underline{\sigma}}_2 \mathrm{d}\Omega
$$

$$
= \int_{\Omega_1} \underline{v}_1 \cdot \underline{b}_1 \mathrm{d}\Omega + \dots \int_{\Omega_2} \underline{v}_2 \cdot \underline{b}_2 \mathrm{d}\Omega + \int_{\Gamma_1^{\mathrm{N}}} \underline{v}_1 \cdot \underline{g}_1^{\mathrm{N}} \mathrm{d}\Gamma + \int_{\Gamma_2^{\mathrm{N}}} \underline{v}_2 \cdot \underline{g}_2^{\mathrm{N}} \mathrm{d}\Gamma + \int_{\Gamma_I} (\underline{v}_1 - \underline{v}_2) \cdot \underline{\lambda} \mathrm{d}\Gamma + \int_{\Gamma_I} \underline{\mu} \cdot (\underline{\dot{u}}_1 - \underline{\dot{u}}_2) \mathrm{d}\Gamma \tag{5}
$$

3.2. FEM discretization

In the FEM partition, the displacement is approximated with classical low-order shape functions:

$$\underline{u}_1^h = \sum_{k=1}^{n_{\text{tot}}^{(1)}} N_k \, \mathbf{U}_k^{(1)} \tag{6}$$

with $n_{\text{tot}}^{(1)}$ the total number of nodes in subdomain Ω_1^h, the superscript h being employed for the discrete setting. The shape functions N_k and the unknown displacement vector (whose dimension is equal to d) $\mathbf{U}_k^{(1)}$ are related to node k. In this work, 3D hexahedral finite elements are considered, coupled with 3D hexahedral spectral elements. Only linear element in the FEM partition are considered here (8-node hexahedra). A thorough presentation of the FEM can be found in finite element textbooks, such as in [15] or [16]. The integral terms of the weak form in Eq. (5) for the FEM partition are obtained by adopting a quadrature formula based on the Gauss sampling points in every hexahedral finite element. It leads to the definition of the consistent mass matrix and the stiffness matrix related to the FEM partition.

3.3. SEM discretization

In the SEM partition, the space discretization is done by subdividing the discrete subdomain Ω_2^h into welded non overlapping elements $\Omega_{2,e}^h$; the index e corresponds to a spectral element with $e = 1, \ldots, n_e$, n_e being the number of spectral elements (SE): $\Omega_2^h = \cup_{e=1}^{n_e} \Omega_{2,e}^h$. In the 3D case, the elements are mapped to a reference cube $[-1, 1] \times [-1, 1] \times [-1, 1]$. The shape functions characterized by high-order Lagrange polynomials of degree N are defined in the reference cube. Polynomial degrees higher than 4 are usually adopted. Contrary to the FEM in which the geometric nodes of the elements are the support of the degrees of freedom, that is the 8 vertex points for a linear hexahedron, Gauss–Lobato–Legendre points (GLL) are employed to define high-order Lagrange polynomials as shape functions for the spectral element. The positions in the reference domain $[-1, 1]$ of the GLLs are given by the roots of the first derivative of the Legendre polynomial of degree N, completed with the extremities -1 and 1. In the case of degree $N = 4$, an hexahedral spectral element includes 125 GLL points ($N + 1$ in each direction of the space). The kinematic quantities (displacement, velocity and acceleration) are obtained at the GLL points that are the support of the degrees of freedom in the SEM partition. The displacement is approximated with high-order Lagrange shape functions, providing an improved accuracy in comparison to the FEM regions when smooth solution is concerned:

$$\underline{u}_2^h = \sum_{k=1}^{n_{\text{tot}}^{(2)}} \psi_k \, \mathbf{U}_k^{(2)} \tag{7}$$

with $n_{\text{tot}}^{(2)}$ the total number of GLL points in subdomain Ω_2^h, the shape functions ψ_k and the unknown displacement vector (d dimension) $\mathbf{U}_k^{(2)}$ at the GLL point k.

In comparison to the FEM, for the case $N = 4$ in SEM, the minimal wavelength is generally sampled by 5 GLL points, while for linear FE, the minimal wavelength is generally sampled by 10 points. The integral terms of the weak form in Eq. (5) for the SEM partition are obtained by adopting a quadrature formula based on the GLL points in every spectral element, contrary to the FEM in which the quadrature computation is based on sampling Gauss points, different from the FE nodes. In SEM, since the mass matrix is diagonal by construction, it is convenient to adopt an explicit Newmark time integration to avoid the inversion of the stiffness matrix. In EFISPEC3D code, the stiffness matrix is never computed and stored in memory. Instead, the vector of internal forces is computed and stored in memory at each time step and then used to solve the acceleration in the time marching system. Further details about the SEM for the wave propagation problem can be found in [2] and [3].

3.4. Interface coupling

In the weak form in Eq. (5), the coupling terms involving Lagrange multipliers, are integrated following a standard mortar approach. The standard mortar approach allows for an efficient gluing between non-matching meshes, including also the case of geometrically non-conforming situation, such as curved interfaces. The discrete finite element slave side is denoted by $\Gamma_I^{(1),h}$, whereas the discrete spectral element master side is denoted by $\Gamma_I^{(2),h}$. In our case, the slave and master sides are 2D flat surfaces that are geometrically coincident with the interface Γ_I. The displacement approximation for the two sides is given below:

$$\underline{u}_1^h|_{\Gamma_I^{(1),h}} = \sum_{r=1}^{n^{(1)}} N_r^{(1)} \mathbf{U}_{I,r}^{(1)}$$

$$\underline{u}_2^h|_{\Gamma_I^{(2),h}} = \sum_{l=1}^{n^{(2)}} \psi_l^{(2)} \mathbf{U}_{I,l}^{(2)}$$

(8)

where $N_r^{(1)}$ are the FE linear shape functions on the slave side and $\psi_l^{(2)}$ are the SE shape functions on the master side. $n^{(1)}$ is the number of FE nodes on the slave side ($n^{(1)} < n_{\text{tot}}^{(1)}$), $n^{(2)}$ is the number of GLL points on the master side ($n^{(2)} < n_{\text{tot}}^{(2)}$); the subscript r corresponds to the nodes of the FEM, whereas the subscript l corresponds to the GLL points of the SEM. We used here different subscripts from Eqs. (6) and (7) because we only focus on the approximations on the interface.

The mortar method for gluing subdomains at an incompatible interface requires the definition of the finite-dimensional subspace for the Lagrange multipliers. Following the standard mortar method [11], the approximation of the Lagrange multipliers is expressed on the slave side and the shape functions are assumed to be identical to the FE shape functions $N_j^{(1)}$. Thus, the approximation of the Lagrange multipliers is expressed on the slave side as:

$$\underline{\lambda}^h = \sum_{j=1}^{n^{(1)}} N_j \, \mathbf{\Lambda}_j$$

(9)

where $\mathbf{\Lambda}_j$ are the discrete nodal Lagrange multipliers of dimension d on the FE slave side and N_j are the associated shape functions, matching the FE shape functions.

Now, the weak form of the velocity continuity at the interface is derived from the global weak formulation in Eq. (5). Indeed, we have to prescribe, $\forall \underline{\mu} \in M$:

$$\int_{\Gamma_I^{(1),h}} \underline{\mu} \cdot (\underline{\dot{u}}_1 - \underline{\dot{u}}_2) \, \mathrm{d}\Gamma = 0$$

(10)

After substituting the previous approximations of velocities from both sides and Lagrange multipliers in the above equation, it is shown [17] that the following discrete kinematic equation can be obtained:

$$L_1 \dot{U}_1 + L_2 \dot{U}_2 = 0$$

(11)

where the matrices L_1 and L_2 are composed of nodal blocks defined as:

$$L_1[i,r] = L_{1,ir} I_d = \int_{\Gamma_I^{(1),h}} N_i^{(1)} N_r^{(1)} \, \mathrm{d}\Gamma I_d$$

$$L_2[i,l] = L_{2,il} I_d = - \int_{\Gamma_I^{(1),h}} N_i^{(1)} \psi_l^{(2)} \, \mathrm{d}\Gamma I_d$$

(12)

L_1 matrix is a square $(d \times n^{(1)}) \times (d \times n^{(1)})$ matrix, whereas the matrix L_2 is a rectangular matrix of dimension $(d \times n^{(1)}) \times (d \times n^{(2)})$. In the following, we define $N_I = d \times n^{(1)}$, corresponding to the number of degrees of freedom on the FE slave side. In the works of Ehrl and co-authors [17], the L_1 and L_2 matrices are denoted as D and $-M$ matrices, with D a diagonal matrix thanks to the chosen dual Lagrange multiplier shape functions that are endowed with the biorthogonality property. This alternative method, called dual mortar approach, enables a significant reduction in the total number of degrees of freedom. In this work, the standard mortar approach is preferred, leading to a non-diagonal constraint matrix L_1.

4. SEM/FEM coupling method

4.1. Time integration

After integrating in space the terms in Eq. (5) according to FEM and SEM procedures, the semi-discrete equilibrium equations in both subdomains and the semi-discrete constraint equation can be derived $\forall t \in J = [0, T]$ as:

$$\begin{cases} M_1 \ddot{U}_1(t) + K_1 U_1(t) = F_{\text{ext},1}(t) + L_1^\mathsf{T} \Lambda(t) \\ M_2 \ddot{U}_2(t) + F_{\text{int},2}(t) = F_{\text{ext},2}(t) + L_2^\mathsf{T} \Lambda(t) \\ L_1 \dot{U}_1(t) + L_2 \dot{U}_2(t) = 0 \end{cases}$$

(13)

where $U_1(t)$ and $U_2(t)$ are global vectors related to the subdomains Ω_1 and Ω_2, of dimensions $n_{\text{tot}}^{(1)}$ and $n_{\text{tot}}^{(2)}$, respectively, and L_1 and L_2 are the constraint matrices of dimensions $N_I \times n_{\text{tot}}^{(1)}$ and $N_I \times n_{\text{tot}}^{(2)}$. L_1 and L_2 correspond to the extended versions of the constraint matrices defined in Eq. (12), with zero values at all components of the subdomains that do not

belong to the interface. The FEM consistent mass matrix is denoted by M_1 and the FEM stiffness matrix by K_1, both of dimensions $n_{\text{tot}}^{(1)} \times n_{\text{tot}}^{(1)}$. The SEM mass matrix is noted as M_2 of dimensions $n_{\text{tot}}^{(2)} \times n_{\text{tot}}^{(2)}$. Internal forces, denoted by $F_{\text{int},2}(t)$ in the SEM part, are computed via a quadrature procedure based on the GLL points. Noting that the notation $F_{\text{int},2}(t)$ is preferred in the SEM part because the stiffness matrix is not computed in this part contrary to the FEM part, in which we have: $F_{\text{int},1}(t) = K_1 U_1(t)$. The external forces are denoted by $F_{\text{ext},1}(t)$ and $F_{\text{ext},2}(t)$.

The first equation is the discrete in space equation of motion of the FE subdomain Ω_1, the second equation is the discrete in space equation of motion of the subdomain Ω_2, corresponding to the SE subdomain, and the third equation is the discrete in space velocity weak continuity at the interface through mortar coupling. In the continuous time formulation, imposing any kinematic continuity at the interface leads to the same solution. The situation is different after time discretization, for which one of the kinematic quantities has to be chosen for gluing the subdomains between each other. This is a key point because the goal of this work is to set up a co-simulation strategy in which we want to couple an implicit FEM code, handling the near field of a soil/structure interaction problem, with an explicit SEM code, handling the far field. Therefore, it is crucial to adopt a stable coupling scheme able to couple an implicit time integrator associated with a coarse time step for the FEM part with an explicit time integrator associated with a fine time step for the SEM part.

Based on the FETI approach for transient dynamics, Farhat et al. [18] and Gravouil and Combescure [19,20] proposed a dual Schur method, called GC method, able to couple any Newmark time integrators with their own time step. It was demonstrated that coupling an explicit time integrator, such as the CD (Central Difference) scheme, with an implicit time integrator, such as the CAA (Constant Average Acceleration) scheme, requires a velocity continuity at the interface, otherwise the coupling algorithm becomes unstable. It is important to note that the stability demonstration is carried out in the general case of finite element subdomains following the energy argument, provided by the so-called energy method, proposed by Hughes [15] for demonstrating the stability of hybrid explicit/implicit time integration procedures. The main advantages of the coupling GC method is to deal with heterogeneous time integrators and multi time steps.

The subdomain Ω_1 is integrated in time with an implicit time integration scheme (Constant Average Acceleration scheme), characterized by the parameters $\gamma_1 = 0.5$ and $\beta_1 = 0.25$, whereas the subdomain Ω_2 is handled by an explicit time integration scheme (Central Difference scheme), with the parameters $\gamma_2 = 0.5$ and $\beta_2 = 0$. For this purpose, we define the coarse time scale Δt_1 for the implicit subdomain and the fine time scale Δt_2 for the explicit subdomain with $\Delta t_1 = m \Delta t_2$, m denoting the ratio between the time scales. The discrete in space and time equation of motion is written for the subdomain Ω_1 (FEM part) at the large time scale t_m with $\Delta t_1 = [t_0, t_m]$, while the discrete in space and time equation of motion of the subdomain Ω_2 (SEM part) is written at the fine time scale t_j ($j = 1, 2, \ldots m$) with $\Delta t_2 = [t_{j-1}, t_j]$ as follows:

- subdomain 1 on the coarse time step $\Delta t_1 = [t_0, t_m]$:

$$M_1 \ddot{U}_1^m + K_1 U_1^m = F_1^{\text{ext},m} + L_1^{\mathsf{T}} \Lambda^m \tag{14}$$

- subdomain 2 on the fine time step $\Delta t_2 = [t_{j-1}, t_j]$:

$$M_2 \ddot{U}_2^j + F_2^{\text{int},j} = F_2^{\text{ext},j} + L_2^{\mathsf{T}} \Lambda^j \tag{15}$$

- at the interface, the continuity of velocities is imposed at times t_j (at the fine time scale) for $j = 1, 2, \ldots m$ as:

$$L_1 \dot{U}_1^j + L_2 \dot{U}_2^j = 0 \tag{16}$$

Classical Newmark formulas for integrating in time the equation of motion on a time step $\Delta t = [t_n, t_{n+1}]$ are reminded below:

$$\begin{cases} U^{n+1} = U^{n,p} + \beta \Delta t^2 \ddot{U}^{n+1} \\ \dot{U}^{n+1} = \dot{U}^{n,p} + \gamma \Delta t \ddot{U}^{n+1} \end{cases} \tag{17}$$

with β and γ the classical Newmark parameters and the predictor quantities given by:

$$\begin{cases} U^{n,p} = U^n + \Delta t \dot{U}^n + \Delta t^2 \left(\frac{1}{2} - \beta \right) \ddot{U}^n \\ \dot{U}^{n,p} = \dot{U}^n + \Delta t (1 - \gamma) \ddot{U}^n \end{cases} \tag{18}$$

Then, we introduce the predictor quantities related to the two time scales, that is $\Delta t_1 = [t_0, t_m]$ for subdomain Ω_1 and $\Delta t_2 = [t_{j-1}, t_j]$ for subdomain Ω_2. It leads to the equations of motion for the two subdomains in the form:

$$\begin{cases} \widetilde{M}_1 \ddot{U}_1^m = F_1^{\text{ext},m} - K_1 U_1^{0,p} + L_1^{\mathsf{T}} \Lambda^m \\ M_2 \ddot{U}_2^j = F_2^{\text{ext},j} - F_2^{\text{int},j} + L_2^{\mathsf{T}} \Lambda^j & \text{for } j = 1, 2, \ldots m \\ L_1 \dot{U}_1^j + L_2 \dot{U}_2^j = 0 & \text{for } j = 1, 2, \ldots m \end{cases} \tag{19}$$

with the effective stiffness matrix defined in the subdomain Ω_1 by:

$$\widetilde{M}_1 = M_1 + \beta_1 \Delta t_1^2 K_1 \tag{20}$$

The procedure proposed by Gravouil and Combescure is based on a splitting of the kinematic quantities into two parts: the free and the linked quantities. The free quantities are obtained by only considering the internal and external forces, whereas the linked quantities are obtained by only taking into account the interface loads defined by the Lagrange multiplier vector Λ. If we consider the subdomain Ω_1, the discrete equation of motion is split into two parts as follows:

$$\begin{cases} \widetilde{M}_1 \ddot{U}_1^{\mathrm{free},m} = F_1^{\mathrm{ext},m} - K_1 U_1^{0,p} \\ \widetilde{M}_1 \ddot{U}_1^{\mathrm{link},m} = L_1^{\mathsf{T}} \Lambda^m \end{cases} \tag{21}$$

The complete accelerations are obtained by summing the two parts as: $\ddot{U}_1^m = \ddot{U}_1^{\mathrm{free},m} + \ddot{U}_1^{\mathrm{link},m}$. The same procedure is applied to the subdomain Ω_2 at each time t_j.

Furthermore, the free and linked velocities of the subdomain Ω_1 at t_j are interpolated:

$$\begin{cases} \dot{U}_1^{\mathrm{free},j} = (1 - \frac{j}{m})\dot{U}_1^{\mathrm{free},0} + \frac{j}{m}\dot{U}_1^{\mathrm{free},m} \\ \dot{U}_1^{\mathrm{link},j} = (1 - \frac{j}{m})\dot{U}_1^{\mathrm{link},0} + \frac{j}{m}\dot{U}_1^{\mathrm{link},m} \end{cases} \tag{22}$$

Using the kinematic condition at the interface in Eq. (16) at each time t_j, it is shown that the following interface equation can be derived [19,20,5]:

$$H\Lambda^j = b^j \tag{23}$$

with the interface operator and the right-hand-side vector defined by:

$$\begin{cases} H = \gamma_1 \Delta t_1 L_1 \widetilde{M}_1^{-1} L_1^{\mathsf{T}} + \gamma_2 \Delta t_2 L_2 M_2^{-1} L_2^{\mathsf{T}} \\ b^j = -L_1 \dot{U}_1^{\mathrm{free},j} - L_2 \dot{U}_2^{\mathrm{free},j} \end{cases} \tag{24}$$

The dimension of the interface operator is $N_I \times N_I$, that is, a square matrix depending on the number of degrees of freedom on the FE slave side at the interface, due to the choice in the mortar method to assign Lagrange multipliers to the FE side.

Finally, once obtained the Lagrange multiplier vector at the end time of the time step, linked accelerations are obtained assuming only interface forces at the right-hand side of the discrete equation of motion. Linked displacements and velocities are then derived from Newmark formulas (Eqs. (17) and (18)) and added to the free quantities to complete the fine time step Δt_2.

4.2. SEM/FEM co-simulation

The purpose of this section is to briefly present the adopted codes and how to handle the co-simulation. The goal is to couple the implicit FE code, Code_Aster [14], developed by EDF, with the SE code, EFISPEC3D developed by BRGM. To handle the interface problem given in Eq. (23), an external coupling software has been developed in C language. In order to minimize the modifications of the sources of the different codes, an external coupling software has been set up rather than solving the interface problem in the SE or FE code. Besides solving the interface problem, the coupling software is also in charge of data exchange with the FE and SE codes. The data exchange requires communication between several software running on the same computer. For this purpose, pipes in C language, also called FIFO (First In First Out), are efficient tools. It is important to note that no data are directly exchanged between the FE and SE codes, because the coupling software completely ensures the interface between the different codes. The tasks managed by the different codes and the coupling software can be divided into two stages, an initialization stage, which consists in computing the interface operator H, and a solving stage during the time loop. The initialization stage starts with the creation of the pipes required for data exchange between the FE code, denoted by SDA, the SE code, denoted by SDB, and the coupling software, denoted by CPL. To build the operator H given in Eq. (23), the codes have to send the coordinates of the nodes lying on the interface and the connectivity matrices. Thanks to these data, the CPL will evaluate the shape functions associated with each node and create the constraint matrices L_1 and L_2. Besides the constraint matrices, the CPL also needs the inverse of the dynamic operators $\widetilde{M}_1$ and M_2 to create the matrix H. For this purpose, the CPL sends N_I vectors, denoted by X_i with $i = 1 \ldots N_I$; the X_i vector has a value of 1 for the ith degree of freedom and 0 elsewhere. The FE code builds a field with 0-values for the degrees of freedom that do not belong to the interface. Then the FE code solves the following equation:

$$\widetilde{M}_1 Y_i = X_i \tag{25}$$

Then, the FE code picks out the values of Y_i that correspond to the degrees of freedom on the interface and sends them to the coupling software. This vector Y_i corresponds to the ith column of the matrix $\widetilde{M}_1^{-1}$ needed to evaluate the interface operator. This operation is repeated N_I times, N_I being the number of FE degrees of freedom belonging to the interface. For the SE code, since the matrix M_2 is diagonal, the communication only consists in sending the inverse of the terms of the
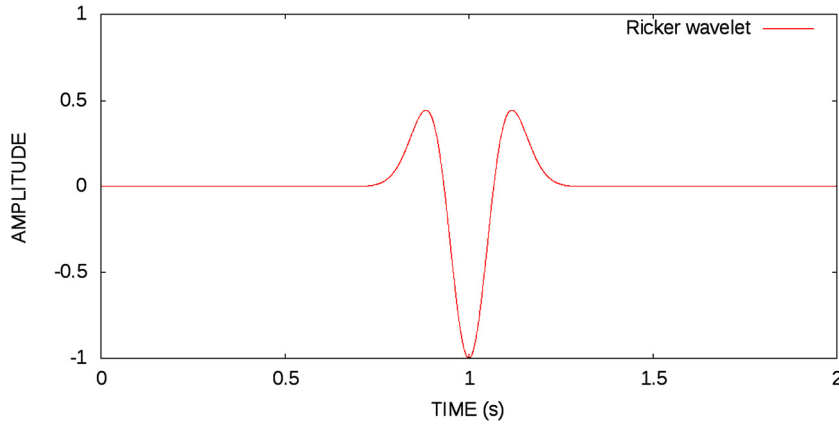
Fig. 2. Ricker wavelet.

matrix corresponding to the degrees of freedom lying on the interface. The coupling software is now able to compute the operator H.

For the time stepping computation, we describe the tasks involved over one macro time step Δt_1:

- solving the free problem on the SDA and sending the free velocities to the CPL;
- starting the loop on the macro time step Δt_1 composed of m micro time steps Δt_2;
- at a given micro time step Δt_2, computing the free quantities in SDB and sending the free velocities to the CPL;
- the CPL receives the velocities from both subdomains and computes the right-hand-side vector b^j in Eq. 24. For the FE subdomain, a linear interpolation is assumed for computing the velocity $\dot{U}_1^{\text{free},j}$ (Eq. 22);
- the CPL solves the interface problem by computing the Lagrange multipliers of dimension $N_I \times 1$ given in Eq. (23);
- the CPL computes the interface forces $F_2^{\text{link},j} = L_2^T \Lambda^j$ and sends them to SDB;
- solving the linked problem on SDB and completing the micro time step Δt_2 by adding up the free and linked quantities;
- proceeding to the following micro time step Δt_2;
- completing the loop over the macro time step Δt_1;
- solving the linked problem on SDA and completing the macro time step Δt_1 by adding up the free and linked quantities after receiving the interface forces $F_1^{\text{link},m} = L_1^T \Lambda^m$.

Figures illustrating the computation tasks and data exchange during co-simulation can be found in previous works [6]. It is interesting to note that, for one macro time step Δt_1, the CPL communicates m times with SDB, but only once with SDA.

5. Numerical examples

In the following applications, non harmonic waves will be investigated by considering a Ricker wave, denoted by *Ric*, defined as:

$$Ric\,(t,\,t_{\mathrm{p}},\,t_{\mathrm{s}}) = A\,(2\,\pi^2\,\frac{(t - t_{\mathrm{s}})^2}{t_{\mathrm{p}}^2} - 1)\,\exp(-\pi^2\frac{(t - t_{\mathrm{s}})^2}{t_{\mathrm{p}}^2}) \tag{26}$$

The Ricker wave is characterized by three parameters: the fundamental period t_{p}, the time shift t_{s} and the amplitude A. The Ricker wave is shown in Fig. 2 for the following parameters: $t_{\mathrm{p}} = 0.3$ s, $t_{\mathrm{s}} = 3$ s and $A = 1$. In SEM, all the numerical experiments are undertaken with polynomial order $N = 4$, which means 5 GLL points in one direction and 125 GLL points in one hexahedron.

5.1. FEM/SEM bar test

The 3D model represents a simple homogeneous bar of 700 m in length and with a section of 10×10 m. A part of the column, of 200 m in length, is dealt with the FEM and the rest (of 500 m in length) with the SEM. The mesh shown in Fig. 3 is only composed of hexahedral elements. This column is subjected to a Ricker P-wave imposed at the right end side of the FE subdomain, with the following characteristics: $t_{\mathrm{p}} = 0.03$ s, $t_{\mathrm{s}} = 0.05$ s, and $A = 1$ MN. The left end side is free. The mechanical characteristics of the linear elastic material are: Young's modulus $E = 30$ GPa, Poisson's ratio $\nu = 0.2$, and density $\rho = 2500$ kg/m^3. The aim of this simple test case is to validate the wave transmission at the interface.

For a Ricker wavelet, the maximum frequency can be assessed by $f_{\max} = 2.5\,f_{\mathrm{p}} = 2.5\frac{1}{t_{\mathrm{p}}}$. The minimum P wavelength is obtained by: $\lambda = v_{\mathrm{p}}/f^{\max}$, with v_{p} the pressure-wave velocity. Here, the pressure-wave velocity is $v_{\mathrm{p}} = 3651$ m/s, and
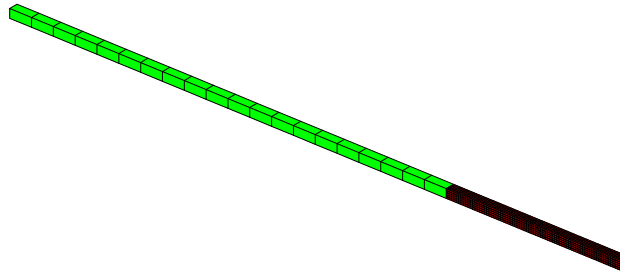
GIBI FECIT

Fig. 3. Decomposed mesh of the bar into two subdomains FEM (fine mesh in red color) and SEM (coarse mesh in green color).

the minimum wavelength is equal to 43.8 m. For ensuring a good accuracy in the SEM partition, we must have at least 5 GLL points to sample the minimal wavelength, which corresponds to a SE size equal or inferior to the wavelength in the case where $N = 4$ (i.e. 5 GLL points along the edges of a SE). Thus, a mesh composed of SE of size $L_{SE} = 25$ m in the longitudinal direction of the bar of 500 m is adopted (approximately 9 GLL points per wavelength). The SE transverse size is equal to 10 m to fit the section. The number of SE elements is 20 with a number of degrees of freedom, $n_{tot}^{(2)}$, equal to 2025. The time step has to be selected based on the critical time step given by the classical CFL condition. For SE elements, the CFL condition depends on the distance between the closest GLL points in one hexahedral element. With the polynomial order $N = 4$, the closest GLL points are distant from a length equal to $\Delta x_{min} = 0.175 \times L_{SE}$, where L_{SE} is the size of the SE. Thus, the CFL condition writes: $\Delta t_2 = 0.59 \Delta x_{min}/v_p$, the coefficient 0.59 corresponding to the Courant number. Here, we consider a time in the explicit SEM part equal to $\Delta t_2 = 0.25$ ms less than the CFL condition, approximately equal to 0.7 ms. Only nested meshes between SE and FE elements are involved: in the cross section, L_{FE} is equal to 2 m, that is, a ratio between the SE and FE sizes $r = L_{SE}/L_{FE} = 5$. The finite element size in the longitudinal direction is equal to 2 m. The time integrator is implicit (constant average acceleration scheme) and unconditionally stable. The time step adopted is either $\Delta t_2 = 0.25$ ms or $\Delta t_2 = 1$ ms in order to assess the validity of the multi time step coupling. This simple co-simulation test is carried out by coupling EFISPEC3D (SEM) with Code_Aster (FEM). In order to validate our co-simulation approach, two full-FEM analyses are performed by employing $\Delta t = 0.25$ ms and $\Delta t = 1$ ms. In these reference cases (without coupling), the same FE sizes previously shown for the FE subdomain (of 200 m in length) are adopted for the whole bar of 700 m in length. The recording point for comparing the kinematic quantities from the two approaches, SEM/FEM coupling approach and full-FEM approach, is located in the middle of the FEM part illustrated in Fig. 3.

In Fig. 4, the wave recorded in the middle of the SEM part is shown: as the force is applied at the right end, the first recorded wave corresponds to 100 m of wave propagation into the medium, the next peak corresponds to the return of the wave after being reflected at the left free end (1200 m of propagation), and the close in time following wave to the return of the wave after reflecting at the right end (200 m of propagation), and so on. From Fig. 4, the accuracy of the coupling SEM/FEM approach is highlighted: the Ricker wave propagates through the two subdomains, almost without any disturbances.

The discrepancies between the results from SEM/FEM co-simulation and full FEM simulation are quantified in terms of error in displacement on the interface, defined by: $err_u(t) = \sqrt{\sum_{i=1}^{n^{(1)}}(u_{SEM-FEM}(t) - u_{ref}(t))^2}$, $n^{(1)}$ being the number of FE nodes at the interface. The error is plotted versus time in Fig. 5. It can be seen that the error increases at each wave passage due to both coupling method and inherent numerical dispersion during the wave propagation of the investigated numerical methods (FEM and SEM). The error remains less than $7 \cdot 10^{-5}$ after the sixth wave passage, corresponding to a relative error of 4%. Next, the isovalues of the displacement can be visualized on the interface for the two results in Fig. 6, at the time corresponding to the first peak in displacement (at around 0.100 s in Fig. 4), along with the relative error map between the two results. It can be seen that the displacement is quite homogeneous in the interface section, with values from $1.67 \cdot 10^{-4}$ to $1.70 \cdot 10^{-4}$, because of the 1D propagation problem, and the relative error remains very low at this first wave passage, with a relative error less than 0.07% in displacement.

Now, the SEM/FEM approach is applied in the case of different time steps, with a time step ratio $m = \Delta t_1/\Delta t_2 = 4$. The recorded displacements are compared in Fig. 7. The first passage of the wave in the middle of the FEM part is well reproduced, whereas some discrepancies can be observed for the next passages: the wave form is slightly altered due to the adopted space and time discretization. Two full-FEM analyses are conducted in order to provide reference results without coupling. It can be noted that the wave is more altered in the case of the full-FEM analysis with a time step equal to 1 ms than in our SEM/FEM case with the same time step in the implicit FE part (1 ms) and the CFL condition in the SE part (0.25 ms). Furthermore, the number of degrees of freedom is less in the case of SEM/FEM than in the case of the full-FEM analysis.

As a conclusion, this first numerical application highlights the fact that, for the same size of problem, it is much more interesting to consider a SEM/FEM coupling approach than a full-FEM approach.
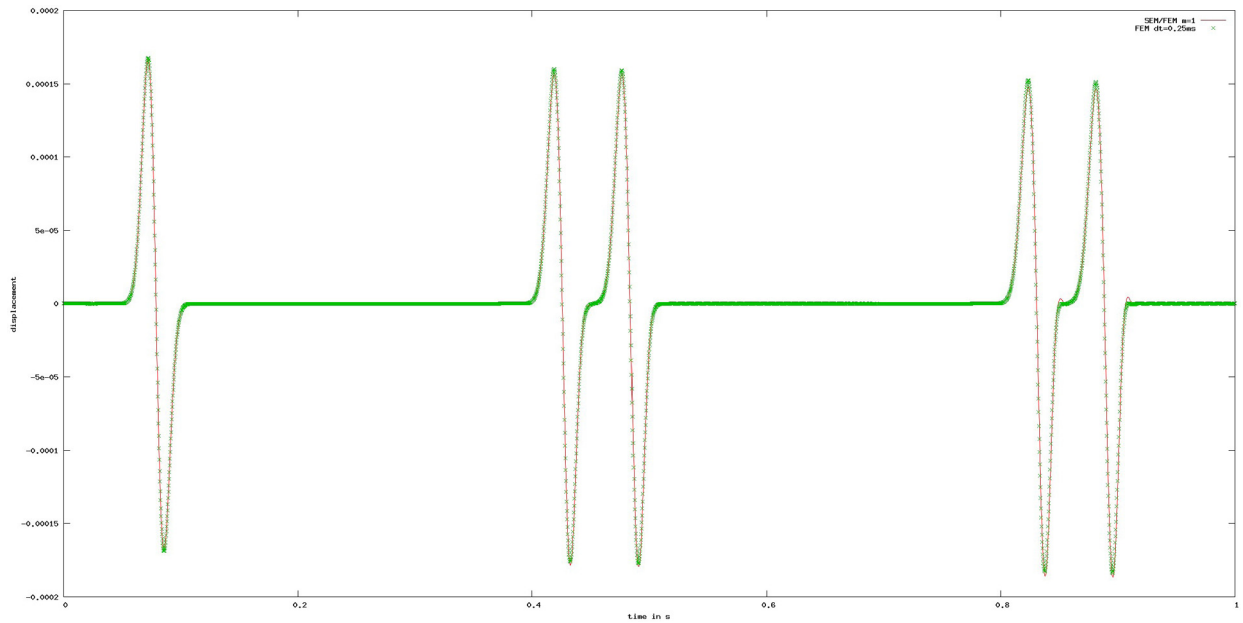
Fig. 4. Comparison in terms of displacement in the middle of the FEM part: SEM/FEM approach versus FEM approach in the case of a homogeneous time step $\Delta t_1 = \Delta t_2 = 0.25$ ms.
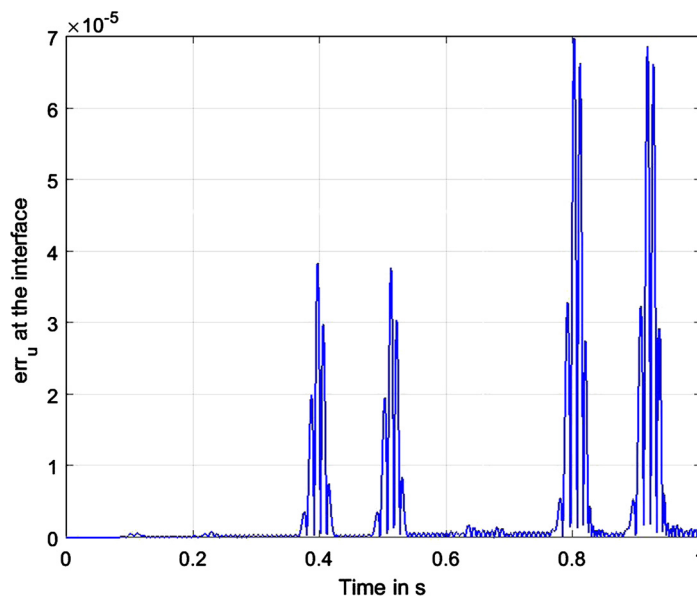

Fig. 5. Time history of the displacement error err_u between SEM/FEM and FEM approaches in the case of homogeneous time step $\Delta t_1 = \Delta t_2 = 0.25$ ms.

5.2. SEM/FEM pseudo-2D test

This model represents a slice of an homogeneous earth medium. The SE mesh is given in Fig. 8. This test case is called pseudo-2D because only one SE is used to represent the section (Y-direction) of the model. For SEM/FEM coupling, we consider an hybrid mesh, meaning that a small part of the medium is modeled with FEs and the rest with SEs. This leads to a simple interface between FE and SE subdomains with the choice of nested meshes between the subdomains, as illustrated in Fig. 9: three faces between the SE and FE partitions have to be taken into account (bottom, right, and left faces), and the ratio between the SE and FE sizes, denoted by r, is varied in the range from 10 to 50. A point source of seismic excitation is placed in the middle of the SE region and the recording point for comparison purpose is located in the middle of the FE region.
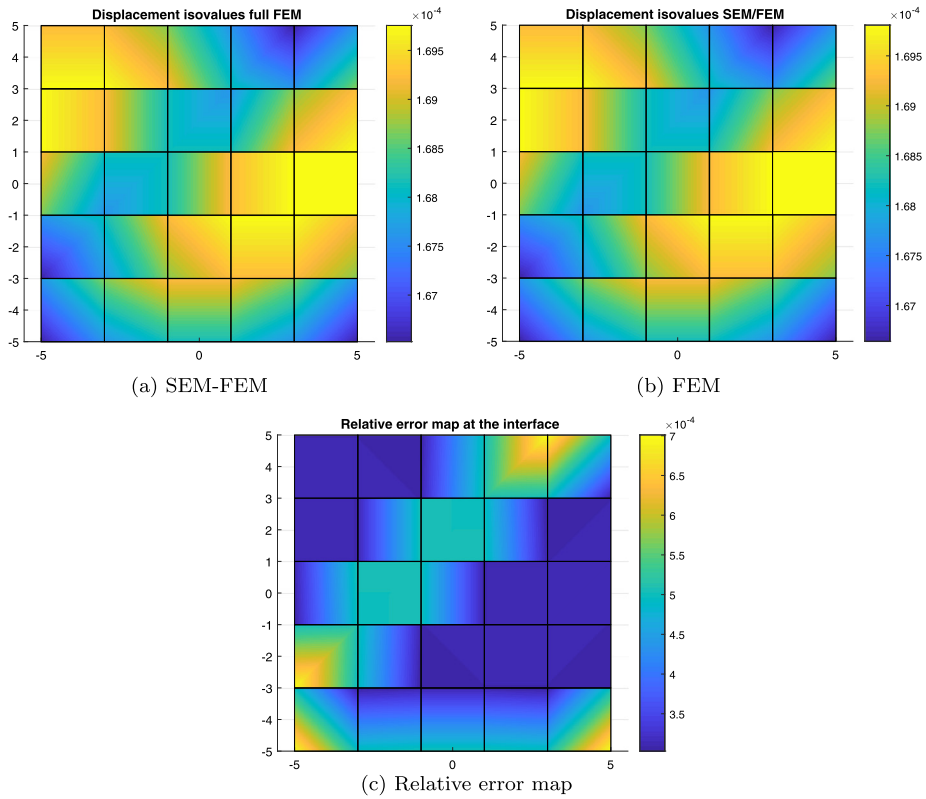
(a) SEM-FEM

(b) FEM

(c) Relative error map

Fig. 6. Displacement and relative error isovalues at the first peak displacement on the interface between the SEM and FEM partitions versus the reference results obtained from the full FEM.
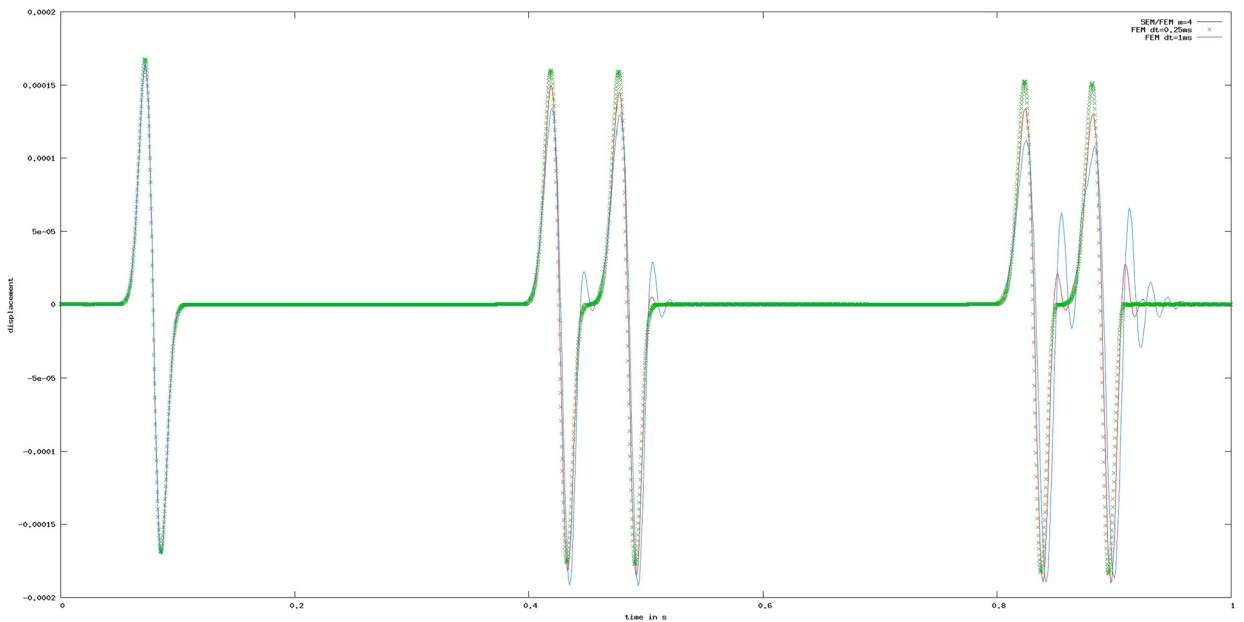

Fig. 7. Comparison in terms of displacement in the middle of the FEM part: SEM/FEM approach versus FEM approach in the case of a heterogeneous time step $\Delta t_1 = m\Delta t_2 = 1$ ms, with $m = 4$.
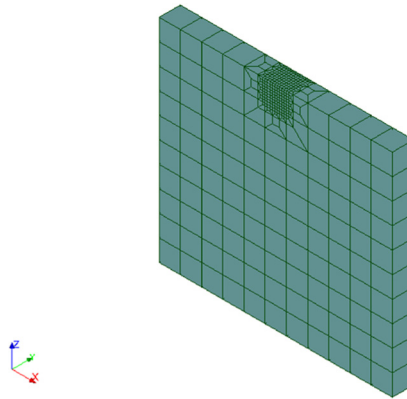
Fig. 8. SE mesh for full-SEM computation; the point source is located in the middle of the SE partition.

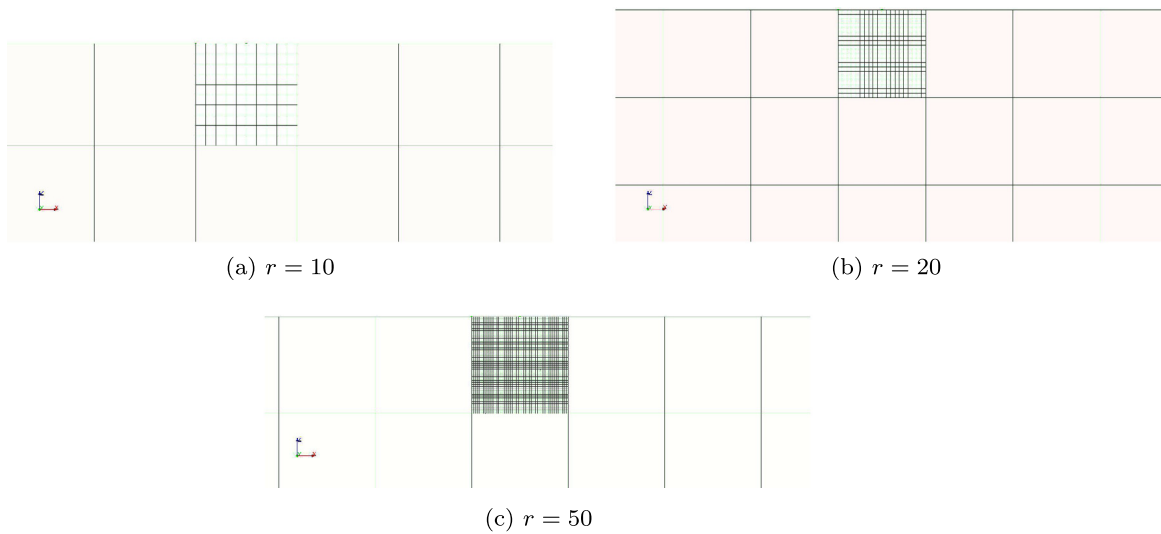
(a) $r = 10$

(b) $r = 20$

(c) $r = 50$

Fig. 9. Zoom on the FEM partition for the SEM/FEM pseudo-2D test for different mesh ratios $r = L_{SE}/L_{FE}$; the small partition, corresponding to the FE partition, is refined; the point source is located in the middle of the SE partition, whereas the receiver point is located in the middle of the FE partition.

No absorbing boundary conditions are introduced. The wave is a Ricker wavelet, with parameters $t_s = 1$ s, $t_p = 0.3$ s, and $A = 1$ MN. The P-wave and S-wave velocities in the SE subdomain are $v_s = 1000$ m/s and $v_p = 1800$ m/s with the density $\rho = 2300$ kg/m^3. The maximum frequency of the Ricker wavelet f_{max} being equal to 8.3 Hz, the SE size should be less than the minimum wave length, that is v_s/f_{max}. The adopted SE size, equal to 100 m, is kept constant in the following and the time step, satisfying the CFL condition, is equal to 2.5 ms. In the FE subdomain, an accuracy equivalent to the one obtained in the previous SE subdomain is achieved if the FE size is taken less than the minimum wavelength divided by 10, that is $v_s/(10 f_{max})$. As we consider finer and finer FE meshes ($r = L_{SE}/L_{FE}$ varying from 10 to 50), we want to keep the same spatial accuracy in the FE subdomain by satisfying exactly this previous relationship. For example, for the case $r = 10$, we have exactly: $L_{FE} = v_s/(10 f_{max})$, taking into account same material characteristics in FE subdomain as in SE subdomain as given in Table 1. Now, if we refine the FE mesh, the accuracy in the FE subdomain becomes better than in the SE subdomain. Thus, we tuned Young's modulus in the FE subdomain in order to maintain the same level of accuracy than in the SE subdomain (Poisson's ratio being constant and equal to 0.277) as shown in Table 1. Thus, the cases $r = 20$ and $r = 50$ correspond to heterogeneous cases, with soft material in the FE subdomain with respect to the material in the SE subdomain. For all cases, the FE time step is $\Delta t_1 = 5$ ms, irrespective of the FE mesh refinement, due to the implicit time integration. Thus, the time step size in the FE partition is twice the one of the SE partition. For each case (homogeneous case with $r = 10$, and heterogeneous cases with $r = 20$ and $r = 50$), a reference solution is provided by a full-SEM computation for comparison purposes.

Displacements obtained from the hybrid SEM/FEM computation are checked versus the full SEM computation at a receiver point located in the middle of the FE region. As shown in Fig. 10, the agreement between the two results is very good. Small discrepancies can be observed for the case $r = 50$ after 4 s, but, even for this large ratio between the SE and FE sizes, the SEM/FEM prediction is very close to the reference results. From theses results, we can conclude that the proposed

Table 1
Material parameters for the FE subdomain depending on the refinement of the mesh (ratio r).

Ratio r	FE size L_{FE} in m	Young's modulus E in MPa	Poisson's ratio ν	S-wave velocity v_s in m/s
10	10	5873	0.277	1000 m/s
20	5	1468	0.277	500 m/s
50	2	235	0.277	200 m/s

(a) $r = 10$

(b) $r = 20$

(c) $r = 50$
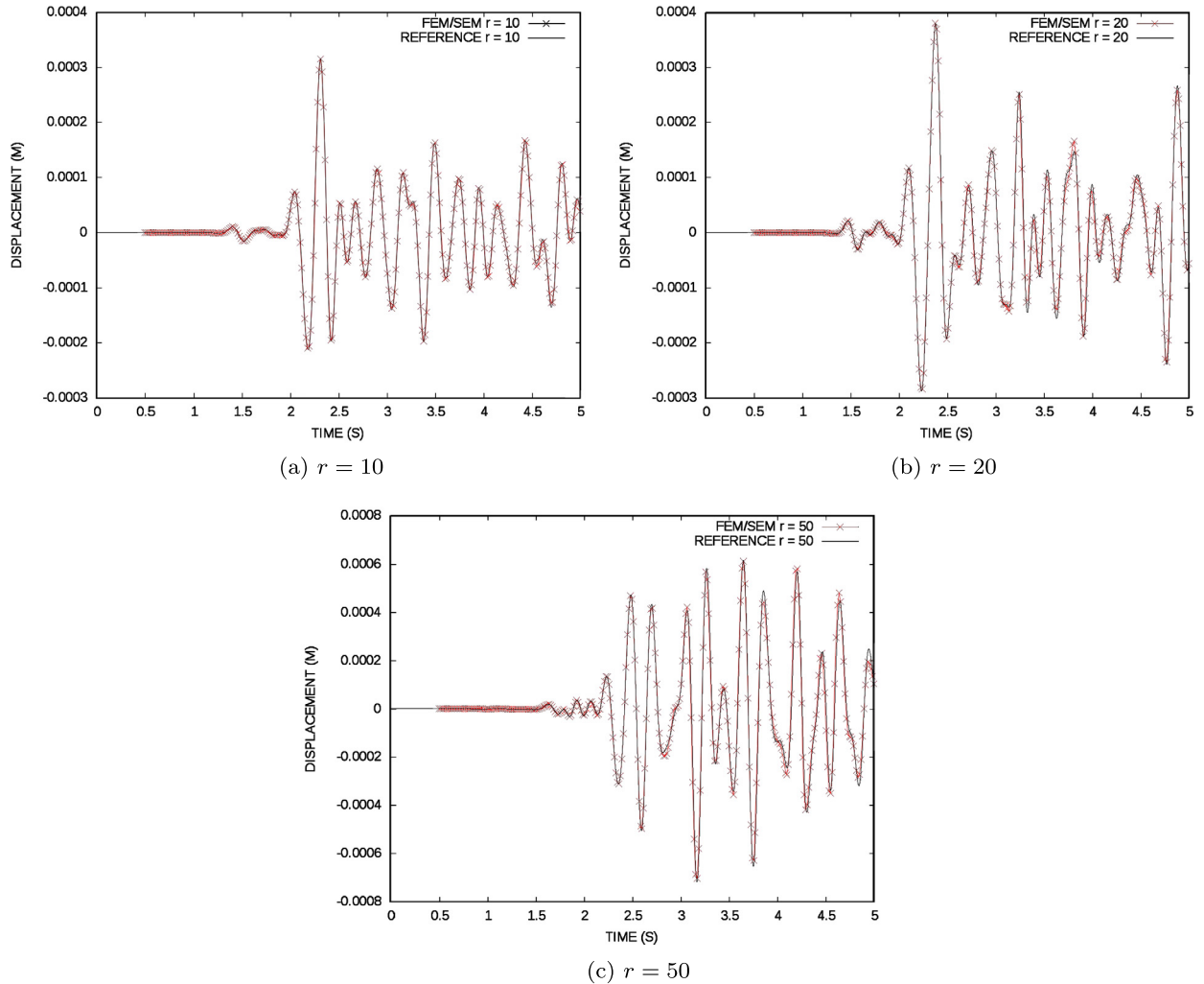
Fig. 10. Comparison of horizontal displacements between SEM/FEM and full SEM (reference) results at a point located in the middle of the FE partition for different ratios $r = L_{SE}/L_{FE}$.

coupling SEM/FEM method is able to deal with large differences in FE and SE sizes at the interface between the SE and FE partitions.

5.3. SEM/FEM full 3D test

This numerical experiment represents a 3D earth medium. As in the pseudo-2D test case, a small part of the medium is dealt with the FEM and the rest with the SEM. A point source of seismic excitation is placed in the middle of the SE region. No absorbing boundary conditions are taken into account. The wave is a Ricker wavelet, with the parameters $t_s = 1$ s, $t_p = 0.3$ s, and $A = 1$ MN. The S and P wave velocities are: $v_s = 1000$ m/s and $v_p = 1800$ m/s with the density $\rho = 2300$ kg/m^3. The maximum frequency of the Ricker wavelet is 8.3 Hz, thus we adopt a SE size equal to 100 m and the FE size is equal to 10 m (mesh ratio r equal to 10). The partitioned mesh, composed of SE and FE hexahedral elements, is shown in Fig. 11.
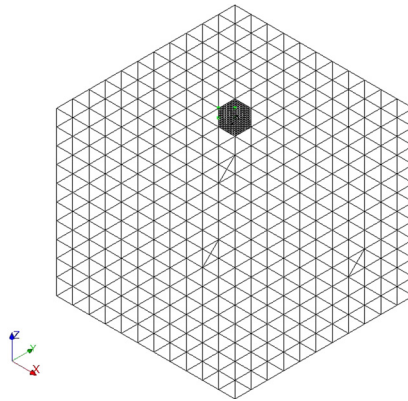
Fig. 11. SE and FE partitions; the small partition corresponds to the FE partition; the point source is located in the middle of the SE partition, whereas the receiver point is located in the middle of the FE partition.
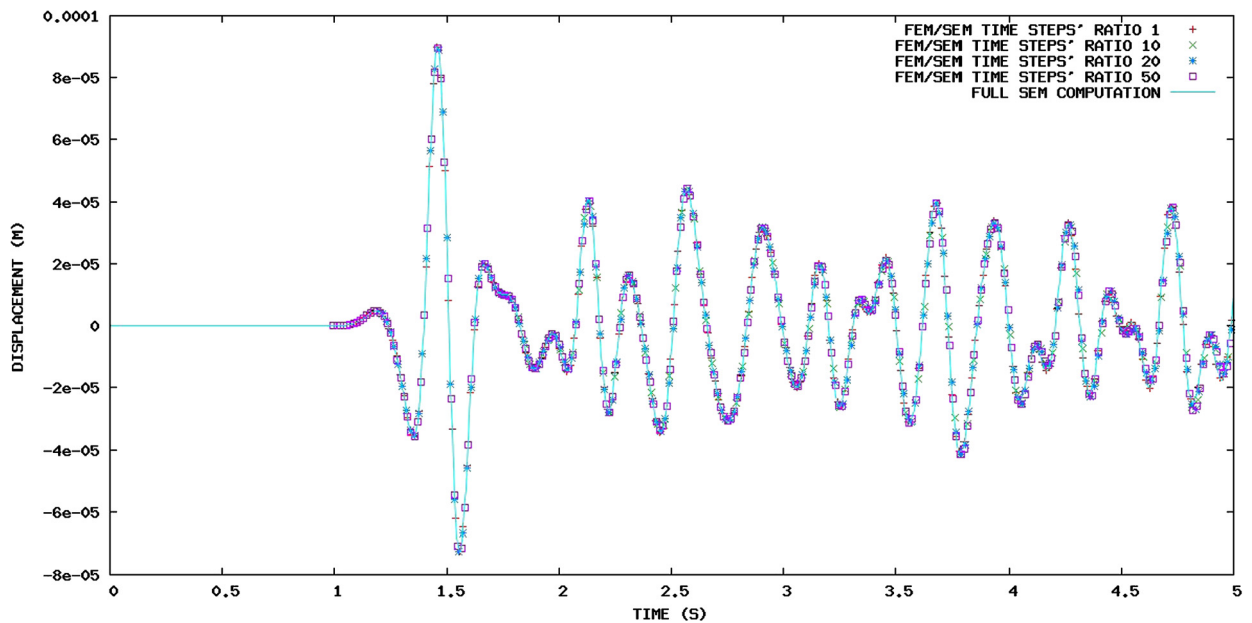

Fig. 12. Comparison between SEM/FEM and full SEM (reference) results at a point located in the middle of the FE partition for different time step ratios $m = \Delta t_1/\Delta t_2$: horizontal displacements in the X direction.

This case presents an interface with more faces than the previous test case (five faces in this case instead of three faces in the pseudo-2D case). In this test, we investigate also the effect of the time step ratio between the two subdomains. Several calculations are performed with different time step ratios m varying from 5 to 50. The time step in the FE region is kept constant and equal to 5 ms. The SE and FE sizes at the interface are kept unchanged for all the simulations. The SE time step is refined in order to check the validity of the proposed hybrid approach for increasing values of the time step ratio m.

The reference solution is the same for all the calculations, and is obtained from a full-SEM calculation. Results in terms of displacements from the hybrid SEM/FEM computation are compared with the reference full-SEM computation in Fig. 12.

The results exhibit a very good agreement between the FEM/SEM co-simulation and the full-SEM reference results, even with a time step ratio equal to 50, which corresponds to a time step of 0.1 ms in the SE subdomain. The CPU times are: 112 s for the coupling software, 117 s for the SEM part, and 131 s for the FEM part, when the time step ratio is equal to 1. The CPU times include waiting times required by data exchange.

As a result, the proposed co-simulation strategy allows us to employ a fine mesh in the FE partition, integrated with an implicit time integrator using a large time step, without changing the mesh and the time step in the explicit SE region. This point is of crucial importance in soil/structure interaction problems, in which it is desirable to dissociate the treatment of the far field by the SEM from that of the near field by the FEM. Thanks to the proposed co-simulation approach, it becomes possible, in a first stage, to set up the SE simulation for the large earth medium and, in a second stage, to tune the FE near field simulation, including the structure and the surrounding soil, by using the appropriate mesh and time step.

6. Conclusion

In order to deal with 3D complex soil/structure interaction problems, a multi time step FEM/SEM co-simulation has been proposed in this paper, able to couple in the same simulation a SEM code, EFISPEC3D, devoted to the wave propagation into very large earth media, with an industrial FEM code, Code_Aster, suitable for modeling complex geometries, such as the structure and the surrounding soil layers. The common weak form of the wave propagation problem in a domain divided into two partitions is first presented, from which the spatial FEM and SEM discretizations are derived. At the interface between FEM and SEM partitions, a mortar method is adopted, allowing us to handle geometric non-conformity, corresponding to the incompatible FEM and SEM meshes at the interface, as well as algebraic non-conformity, due to very different polynomial degrees of the shape functions employed in FEM and SEM partitions. Then an hybrid (different time integrators) and asynchronous (different time steps) time integrator is adopted in order to couple the explicit SEM with an implicit FEM, while keeping the appropriate time step size in the different partitions. Finally, the explicit/implicit multi time step co-simulation, coupling EFISPEC3D code with Code_Aster, has been validated in comparison to full-SEM approach for simple 3D soil interaction problems.

As a conclusion, the proposed methodology is very promising for modeling soil/structure interaction with a wide earth medium, including details of an earthquake source and details of the site of study (fine meshed sedimentary basin and structure with its foundation), thanks to the good accuracy of the spectral element method for wave propagation from the source to the site and the flexibility offered by the finite element method for building simulation with its surrounding soil. Work is in progress for testing more complex soil/structure interaction problems (realistic large earth medium and structure) as well as introducing non-linearities in the FEM partition. In addition, other hybrid asynchronous time integrators could be explored such as the weak coupling in time recently proposed [9,10], enabling to adopt more advanced time integrators such as α methods for damping out the spurious high frequencies due to finite element discretization.

References

[1] A.T. Patera, A spectral element method for fluid dynamics: laminar flow in a channel expansion, J. Comput. Phys. 54 (1984) 468–488.

[2] D. Komatitsch, J.P. Vilotte, R. Vai, J.M. Castillo-Covarrubias, F.J. Sanchez-Sesma, The spectral element method for elastic wave equations – applications to 2-d and 3-d seismic problems, Int. J. Numer. Methods Eng. 45 (1999) 1139–1164.

[3] D. Komatitsch, J. Tromp, Introduction to the spectral element method for three-dimensional seismic wave propagation, Geophys. J. Int. 139 (1999) 806–822.

[4] M. Brun, A. Batti, A. Limam, A. Gravouil, Explicit/implicit multi-time step co-computations for blast analyses on a reinforced concrete frame structure, Finite Elem. Anal. Des. 52 (2012) 41–59.

[5] M. Brun, A. Batti, A. Limam, A. Combescure, Implicit/explicit multi-time step co-computations for predicting reinforced concrete structure response under earthquake loading, Soil Dyn. Earthq. Eng. 33 (2012) 19–37.

[6] M. Brun, A. Batti, A. Combescure, A. Gravouil, External coupling software based on macro- and micro-time scales for explicit/implicit multi-time-step co-computations in structural dynamics, Finite Elem. Anal. Des. 86 (2014) 101–119.

[7] J. Nunez-Ramirez, J.-C. Marongiu, M. Brun, A. Combescure, A partitioned approach for the coupling of SPH and FE methods for transient nonlinear FSI problems with incompatible time-steps, Int. J. Numer. Methods Eng. 109 (2017) 1391–1417.

[8] F.-E. Fekak, M. Brun, A. Gravouil, B. Depale, A new heterogeneous asynchronous explicit–implicit time integrator for nonsmooth dynamics, Comput. Mech. 60 (1) (2017) 1–21, https://doi.org/10.1007/s00466-017-1397-0.

[9] M. Brun, A. Gravouil, A. Combescure, A. Limam, Two FETI-based heterogeneous time step coupling methods for Newmark and alpha-schemes derived from the energy method, Comput. Methods Appl. Mech. Eng. 283 (2015) 130–176.

[10] A. Gravouil, A. Combescure, M. Brun, Heterogeneous asynchronous time integrators for computational structural dynamics, Int. J. Numer. Methods Eng. 102 (2015) 202–232.

[11] C. Bernardi, N. Debit, Y. Maday, Coupling finite element with spectral methods: first results, Math. Comput. (1990) 21–39.

[12] F. Casadei, E. Gabellini, G. Fotia, F. Maggio, A. Quarteroni, A mortar spectral/finite element method for complex 2d and 3d elastodynamics, Comput. Methods Appl. Mech. Eng. (2002) 5119–5148.

[13] F. De Martin, Verification of spectral-element method code for the southern California earthquake center LOH. 3 viscoelastic case, Bull. Seismol. Soc. Amer. 101 (2011) 2855–2865.

[14] Code_Aster, Structures and Thermomechanics Analysis for Studies and Research, EDF, https://www.code-aster.org.

[15] T.J.R. Hughes, The Finite Element Method: Linear Static and Dynamic Finite Element Analysis, Prentice-Hall, Englewood Cliffs, NJ, USA, 1987.

[16] O.C. Zienkiewicz, R.L. Taylor, Finite Element Method, McGraw-Hill Companies, 1989.

[17] A. Ehrl, A. Popp, V. Gravemeier, W.A. Wall, A dual mortar approach for mesh tying within a variational multiscale method for incompressible flow, Int. J. Numer. Methods Eng. 76 (2014) 1–27.

[18] C. Farhat, L. Crivelli, F.X. Roux, Transient FETI methodology for large-scale parallel implicit computations in structural mechanics, Int. J. Numer. Methods Eng. 37 (1994) 1945–1975.

[19] A. Gravouil, A. Combescure, A multi-time-step explicit–implicit method for non-linear structural dynamics, Int. J. Numer. Methods Eng. 50 (2001) 199–225.

[20] A. Combescure, A. Gravouil, A numerical scheme to couple subdomains with different time-steps for predominantly linear transient analysis, Comput. Methods Appl. Mech. Eng. 191 (2002) 1129–1157.